IEEE TRANSACTIONS ON POWER ELECTRONICS, VOL. 39, NO. 12, DECEMBER 2024

Control Strategy of a Hybrid SiC-Si Traction Inverter for Direct-Drive Multiphase PMSMs in Marine Propulsion

Shusen Ni, *Student Member, IEEE*, Chi Li, *Member, IEEE*, and Zedong Zheng, *Senior Member, IEEE*

***Abstract*—This article introduces a novel inverter structure tailored for direct-drive marine propulsion applications, integrating SiC-MOS and Si-IGBT devices in a hybrid bridge arm configuration. The scheme aims to enhance torque control performance by raising the switching frequency of the SiC-MOS and to minimize losses in the propulsion system by lowering the switching frequency of the Si-IGBT. Methods for torque ripple suppression and efficiency enhancement are proposed in this paper. The latter includes introducing the optimal switching frequency combination (OSFC) and optimized load distribution (OLD) methods. The OSFC method aims to determine the optimal combination of switching frequencies for Si-IGBT devices relative to the predetermined frequency of SiC-MOS devices, thereby maximizing system efficiency at the rated torque operating point. On the other hand, the OLD method adjusts the load distribution between the motor windings of SiC-MOS and Si-IGBT devices to enhance the propulsion system's efficiency, particularly under light load conditions. Moreover, experimental validation of the proposed methods is provided. Experimental results show that the proposed control strategy can reduce total drive system losses by 30% compared to an all-Si-IGBT inverter and save 35% in costs compared to an all-SiC-MOS inverter while maintaining torque control performance.**

***Index Terms*—Control strategy, hybrid SiC-Si, marine propulsion, multiphase motor, optimal efficiency, torque ripple suppression.**

NOMENCLATURE

Acronyms

SiC-MOS	Silicon carbide metal-oxide-semiconductor field-effect transistor.
Si-IGBT	Silicon insulate-gate bipolar transistor.
OSFC	Optimal switching frequency combination.
OLD	Optimized load distribution.
EMF	Electromotive force.

Variables

m	Number of SiC-MOS bridge arms.
n	Number of Si-IGBT bridge arms.
$f_{\mathrm{s\text{-}SiC}}$	Switching frequency of SiC-MOS devices.
$f_{\mathrm{s\text{-}Si}}$	Switching frequency of Si-IGBT devices.
$I_{\mathrm{pk}(1)}$	Phase current amplitude in SiC-MOS.
$I_{\mathrm{pk}(2)}$	Phase current amplitude in Si-IGBT.
$R_{\mathrm{DS,ON}}$	On-state resistance of SiC-MOS from drain to source.
$R_{\mathrm{SD,ON}}$	On-state resistance of SiC-MOS from source to drain.
V_{BD}	Knee voltage of the body diode in SiC-MOS.
R_{BD}	On-resistance of the body diode in SiC-MOS.
$T_{\mathrm{d,SiC}}$	Dead time of SiC-MOS devices.
$T_{\mathrm{ON,SiC}}$	Switching-ON time of SiC-MOS devices.
$T_{\mathrm{OFF,SiC}}$	Switching-OFF time of SiC-MOS devices.
V_{CE0}	Collector-emitter threshold voltage.
R_{CE}	On-resistance of the Si-IGBT.
V_{D}	Knee voltage of the antiparallel diode.
R_{D}	On-resistance of the antiparallel diode.
$T_{\mathrm{d,Si}}$	Dead time of Si-IGBT devices.
$T_{\mathrm{ON,Si}}$	Switching-ON time of Si-IGBT devices.
$T_{\mathrm{OFF,Si}}$	Switching-OFF time of Si-IGBT devices.
M	Modulation index.
φ	Angle between phase voltage and current.
$P_{\mathrm{con,F}}$	Forward conduction loss of SiC-MOS.
$P_{\mathrm{con,R}}$	Reverse conduction loss of SiC-MOS.
$P_{\mathrm{dead,BD}}$	Body diode conduction loss during dead time of SiC-MOS.
$P_{\mathrm{sw,SiC}}$	Switching loss of SiC-MOS.
$P_{\mathrm{SiC\text{-}MOS}}$	Overall losses of SiC-MOS.
$P_{\mathrm{con,T}}$	Forward conduction loss of Si-IGBT.
$P_{\mathrm{con,D}}$	Antiparallel diode reverse conduction loss of Si-IGBT.
$P_{\mathrm{dead,D}}$	Antiparallel diode conduction loss during dead time of Si-IGBT.
$P_{\mathrm{sw,Si}}$	Switching loss of Si-IGBT.
$P_{\mathrm{Si\text{-}IGBT}}$	Overall losses of Si-IGBT.
P_{Cu1}	Copper loss caused by the fundamental current.
P_{Cu2}	Copper losses caused by the low harmonics of the current.
P_{Cu3}	Copper losses caused by high-frequency PWM current harmonics.

Manuscript received 19 March 2024; revised 13 June 2024; accepted 14 July 2024. Date of publication 29 July 2024; date of current version 7 October 2024. This work was supported by the National Natural Science Foundation of China under Grant U2106217. Recommended for publication by Associate Editor K-B. Lee. *(Corresponding author: Zedong Zheng.)*

The authors are with the State Key Lab of Control and Simulation of Power Systems and Generation Equipments, Department of Electrical Engineering, Tsinghua University, Beijing 100084, China (e-mail: nss22@mails.tsinghua.edu.cn; chi.li.2014@ieee.org; zzd@mail.tsinghua.edu.cn).

Color versions of one or more figures in this article are available at https://doi.org/10.1109/TPEL.2024.3434703.

Digital Object Identifier 10.1109/TPEL.2024.3434703

P_{Cu}	Overall copper losses.
R_{s}	Stator resistor of the multiphase motor.
L_{s}	Stator inductance of the motor.
ω_1	Fundamental angular frequency of phase current.
ωc	Carrier angular frequency.
ω	Electrical angular velocity.
ω_m	Mechanical angular velocity.
θ_c	Initial angle of the carrier.
p	Carrier signal index.
q	Modulating signal index.
Jq	Bessel function of the first kind.
sign	Sign function.
i_k	Current in phase k.
I_h	Amplitude of hth current harmonic.
φ_h	Initial phase of hth current harmonic.
α_k	Position of phase k to the first phase.
e_k	EMF in phase k.
E_v	Amplitude of vth EMF harmonic.
ψ_v	Initial angle of hth EMF harmonic.
$I*_{11}$	Amplitude of injected 11th harmonic current.
$\varphi*_{11}$	Initial angle of injected 11th harmonic current.
$\boldsymbol{i}_{\mathrm{ABC}}$	Current in the set of winding where the SiC-MOS bridge arm is located.
$\boldsymbol{i}_{\mathrm{UVW}}$	Current in the set of winding where the Si-IGBT bridge arm is located.
θ	Rotor position angle.
$\boldsymbol{i}\alpha\beta$	Overall current vector in the α_1-β_1 subspace of the two sets of windings.
d	Current distribution factor.
$\boldsymbol{i}^{(1)}{}_{\alpha\beta}$	Current vector in the α_1-β_1 subspace of the first set of windings with SiC-MOS.
$\boldsymbol{i}^{(2)}{}_{\alpha\beta}$	Current vector in the α_1-β_1 subspace of the second set of windings with Si-IGBT.
$\boldsymbol{i}^{(1)}{}_{\mathbf{dq}}$	Current in the dq frame of the first set of windings with SiC-MOS.
$\boldsymbol{i}^{(2)}{}_{\mathbf{dq}}$	Current vector in the dq frame of the second set of windings with Si-IGBT.
$\boldsymbol{i}^{(1)*}{}_{\mathbf{dq11}}$	Injected 11th harmonic current in the dq_{11} frame of first set of windings with SiC-MOS.
$\boldsymbol{i}^{(1)*}{}_{\mathbf{dq13}}$	Injected 13th harmonic current in the dq_{13} frame of first set of windings with SiC-MOS.

I. INTRODUCTION

MULTIPHASE motors are increasingly preferred over conventional three-phase motors in electric vehicles, locomotive traction, and ship propulsion due to their smaller per-phase capacity, greater reliability, and reduced torque pulsations [1], [2], [3], [4]. In marine electric propulsion systems, direct-drive multiphase motors are typically integrated directly into the propulsive blades, which commonly operate at low speeds ranging from a few hundred rpm. This aspect forms the focus of the research discussed in this article [5], [6].

Conventional Si-IGBT devices face limitations in high-performance, high-speed motor applications due to their low switching frequency and significant device losses. In contrast, SiC-based devices offer advantages in achieving higher efficiency and power density [7] compared to traditional Si-based devices, owing to their lower losses, higher operating temperature, and increased switching frequency [8], [9], [10]. SiC-based devices are increasingly favored in motor drives, particularly for low-inductance motors, high-speed motors, and high-temperature environment applications. In such scenarios, significant increases in the device's switching frequency can be employed to maintain acceptable levels of current ripple [7], [8].

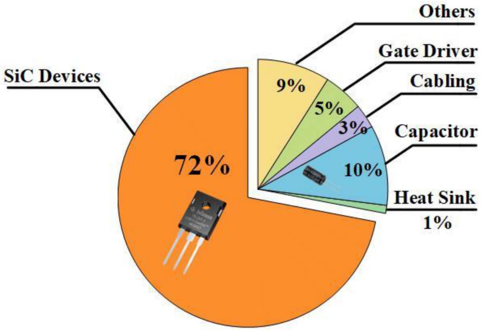

Fig. 1. Breakdown of liquid-cooled SiC-based traction inverter by cost.

The primary challenge in implementing SiC-based inverters is their high cost. For example, the cost breakdown of a liquid-cooled SiC-based inverter is illustrated in Fig. 1, with the expense primarily attributed to the SiC power module (or discrete device), representing 72% of the total [11].

Numerous researchers have endeavored to hybridize Si-IGBT and SiC-MOS devices, aiming to lower the overall cost of SiC-based inverters. Simultaneously, they seek to fully exploit the benefits of both low losses and the high switching frequency inherent in SiC devices [12], [13], [14], [15], [16]. An example is the documented applications of hybrid SiC-MOS and Si-IGBT in three-phase grid-connected systems [16]. Connecting two three-phase SiC-MOS and Si-IGBT inverters to the grid compensate for overall harmonics through the high switching frequency of SiC-MOS. Meanwhile, the switching frequency of Si-IGBT is reduced to minimize losses. It should be noted that the inverter formed by the SiC-MOS bridge legs constitutes only a portion of the rated power. Its primary role is to provide harmonic compensation, ensuring that the total harmonic distortion of the current meets the specified requirements.

In summary, the hybrid schemes employing Si-IGBT and SiC-MOS devices share common characteristics.

1) Utilizing SiC-MOS with lower switching losses compared to Si-IGBTs and operating them in a high switching frequency to ensure the overall output performance, including parameters like total harmonic distortion (THD) of the output voltage or achieving fast dynamic response [12], [13], [17].
2) Allowing Si-IGBT to operate at a lower switching frequency to mitigate switching losses, thereby enhancing the overall efficiency of the converter.

A novel inverter structure incorporating a hybrid SiC-MOS and Si-IGBT bridge arms was proposed in our previous work [18], as depicted in Fig. 2. Considering an asymmetric six-phase

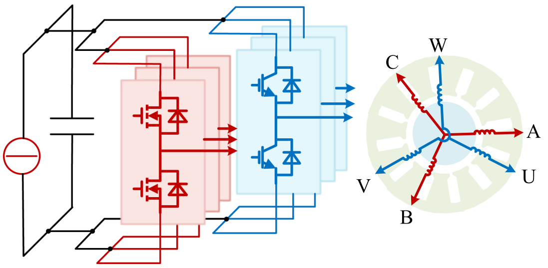

Fig. 2. Proposed inverter with hybrid SiC-MOS and Si-IGBT bridge arms.

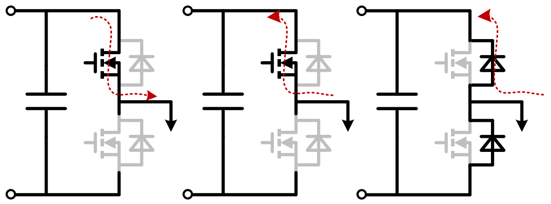
(a) (b) (c)

Fig. 3. Current flow path of SiC-MOS during (a) forward conduction, (b) reverse conduction, and (c) dead time.

motor drive with two neutral points, one set of three-phase windings is powered by the SiC-MOS bridge arms, and the other set is supplied by the Si-IGBT bridge arms. It is challenging to utilize partially rated SiC-MOS bridge arms in a multiphase motor driver due to the motor's uniform winding design. Consequently, the rated capacity of SiC-MOS and Si-IGBT devices should be identical. However, multiphase motors offer increased degrees of freedom for cooperative optimal control between phases due to the magnetic coupling among different phase windings [4].

This research centers on low-speed applications, particularly marine electric propulsion employing permanent magnet direct-drive motors [10], [11], [19]. Within an inverter featuring hybrid SiC-MOS and Si-IGBT bridge arms, torque ripple is suppressed by elevating the switching frequency of the SiC-MOS to enhance control performance while optimizing system efficiency by reducing the switching frequency of the Si-IGBT. The topology and tentative analyses were previously discussed in our earlier work [18]. In this study, we enrich the theoretical analysis and improve the control strategy with thorough experimental verification. The major contributions are made as follows.

1) The article introduces a method for selecting the high switching frequency for SiC-MOS and proposes a method to suppress torque ripple through harmonic injection in the winding set containing SiC-MOS, thereby enhancing the torque control performance.
2) The article presents the OSFC method, which can determine the Si-IGBT switching frequency for optimal system efficiency under the predetermined frequency of SiC-MOS.
3) The propulsion system efficiency is improved by optimizing load distribution between the windings set containing SiC-MOS and the set containing Si-IGBT, especially under light load conditions.

The rest of this article is organized as follows. In Section II, the loss model of the inverter and the multiphase motor are presented, which serves as an optimization basis for the proposed OSFC and optimal load distribution (OLD) problem. In Section III, this article introduces the switching frequency selection method of SiC-MOS, torque ripple compensation method, OSFC method, and OLD method. Additionally, the proposed hybrid bridge arm structure is compared with both all-Si IGBT and all-SiC MOS schemes. The simulation and experimental verification results are given in Section IV. Finally, Section V concludes this article.

II. Loss Model of the Multiphase Inverter and Multiphase PMSM

A. System Loss Analysis

In the propulsion system, consisting of a multiphase motor and a multiphase inverter, the total system losses primarily consist of two parts: 1) motor losses and 2) inverter losses [20], [21], [22]. Both components of losses must be taken into account in the proposed OSFC and OLD methods for optimizing system efficiency.

Inverter losses mainly consist of conduction losses, blanking time losses, and switching losses [23], [24], with the detailed modeling method described in Sections II-B and II-C.

The losses of multiphase permanent magnet synchronous motors (PMSMs) mainly consist of iron losses, copper losses, and eddy current losses of permanent magnets, along with mechanical losses and additional losses [22], [25]. In marine propulsion with low-speed and large torque motors, copper losses account for the absolute majority. Since iron and eddy current losses constitute a relatively small percentage of the total, and the accurate analytical modeling is very complicated, the motor's copper losses are primarily considered [22], [25], [26]. The loss distribution of low-speed high-torque motors is outlined with copper constituting the primary loss at 87% [27], making it reasonable to focus primarily on copper loss. The methodology for modeling copper losses in motors, encompassing both fundamental and harmonic copper losses, will be detailed in Section II-D.

B. Analytical Loss Model for SiC-MOS

The losses of SiC-MOS devices include three main parts: 1) forward and reverse conduction losses of the channel, 2) body diode conduction losses during dead time, and 3) switching losses of the device [7], [23], [28], [29].

For voltage source inverters, the current flows from the drain to the source during the forward conduction of SiC-MOS, as depicted in Fig. 3(a). The conduction loss generated during this process can be derived as

$$P_{\mathrm{con,F}} = 2mR_{\mathrm{DS,on}}\left(\frac{1}{8}+\frac{M\cos\varphi}{3\pi}\right)I_{\mathrm{pk}(1)}^{2}. \tag{1}$$

For SiC-MOS devices, when the current flows through the reverse channel from source to drain, as shown in Fig. 3(b), the reverse conduction loss incurred in this process can be expressed

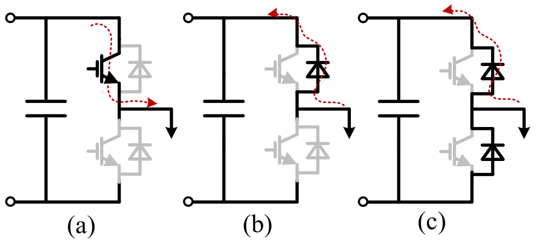

Fig. 4. Current flow path of IGBT during (a) forward conduction, (b) reverse conduction, and (c) dead time.

as

$$P_{\mathrm{con,R}} = 2mR_{\mathrm{SD,on}}\left(\frac{1}{8} - \frac{M\cos\varphi}{3\pi}\right)I_{\mathrm{pk}(1)}^{2}. \tag{2}$$

Another portion of the losses is attributed to the freewheeling of the body diode during the dead time, as in Fig. 3(c) [29], [30]. The loss over this process can be expressed as

$$P_{\mathrm{dead,BD}} = 2m\left(\frac{2V_{\mathrm{BD}}I_{\mathrm{pk}(1)}}{\pi} + \frac{R_{\mathrm{BD}}I_{\mathrm{pk}(1)}^{2}}{2}\right)(T_{\mathrm{d},SiC} - T_{\mathrm{on,SiC}} - T_{\mathrm{off,SiC}})\,f_{\mathrm{s-SiC}}. \tag{3}$$

The switching loss of the devices is mainly related to the load current, bus voltage, and gate resistance. Once the hardware design of the inverter and the bus voltage are determined, the switching loss is predominantly linked with the load current's amplitude [7]. Consequently, the relationship between the total switching energy of the device and the load current is fitted using a polynomial function. This work specifically adopts a quadratic fit, expressing the switching energy as $E_{\mathrm{sw,SiC}}$, which can be derived as

$$E_{\mathrm{sw,SiC}} = a_{\mathrm{SiC}}i^{2} + b_{\mathrm{SiC}}i + c_{\mathrm{SiC}} \tag{4}$$

where a_{SiC}, b_{SiC}, and c_{SiC} represent fitting coefficients for the switching energy, the values of which can be derived by curve fitting from the datasheet [28], [31], [32]. Thus, the total switching loss can be determined as

$$P_{\mathrm{sw,SiC}} = 2m\left(\frac{a_{\mathrm{SiC}}I_{\mathrm{pk}(1)}^{2}}{4} + \frac{b_{\mathrm{SiC}}I_{\mathrm{pk}(1)}}{\pi} + \frac{c_{\mathrm{SiC}}}{2}\right)f_{\mathrm{s-SiC}}. \tag{5}$$

Therefore, the total losses of SiC-MOS are

$$P_{\mathrm{SiC-MOS}} = P_{\mathrm{con},F} + P_{\mathrm{con},R} + P_{\mathrm{dead,BD}} + P_{\mathrm{sw,SiC}}. \tag{6}$$

C. Analytical Loss Model for Si-IGBT

Similar to SiC-MOS devices, the losses of Si-IGBT devices are also comprised of the four components mentioned earlier. However, there is a distinction in that the current flows through the antiparallel diode instead of the reversed channel during the reverse conduction of Si-IGBT [33], [34], [35].

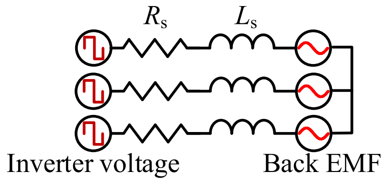

Fig. 5. Steady-state model of one set of three-phase windings of the motor.

The conduction loss of Si-IGBTs during forward conduction, as in Fig. 4(a), is

$$P_{\mathrm{con,T}} = 2n\left(\begin{array}{l}\frac{1}{2}\left(\frac{V_{\mathrm{CE0}}I_{\mathrm{pk}(2)}}{\pi} + \frac{R_{\mathrm{CE}}I_{\mathrm{pk}(2)}^{2}}{4}\right)\\ +M\cos\varphi\left(\frac{V_{\mathrm{CE0}}I_{\mathrm{pk}(2)}}{8} + \frac{R_{\mathrm{CE}}I_{\mathrm{pk}(2)}^{2}}{3\pi}\right)\end{array}\right). \tag{7}$$

In the reverse conduction of Si-IGBT, where the current flows through the antiparallel diode, as illustrated in Fig. 4(b), the loss introduced during this process can be deduced as

$$P_{\mathrm{con,D}} = 2n\left(\begin{array}{l}\frac{1}{2}\left(\frac{V_{\mathrm{D}}I_{\mathrm{pk}(2)}}{\pi} + \frac{R_{\mathrm{D}}I_{\mathrm{pk}(2)}^{2}}{4}\right)\\ -M\cos\varphi\left(\frac{V_{\mathrm{D}}I_{\mathrm{pk}(2)}}{8} + \frac{R_{\mathrm{D}}I_{\mathrm{pk}(2)}^{2}}{3\pi}\right)\end{array}\right). \tag{8}$$

As depicted in Fig. 4(c), during the dead time, the current proceeds through the freewheeling diode, and the loss incurred in this procedure is

$$P_{\mathrm{dead,D}} = 2n\left(\frac{2V_{\mathrm{D}}I_{\mathrm{pk}(2)}}{\pi} + \frac{R_{\mathrm{D}}I_{\mathrm{pk}(2)}^{2}}{2}\right)(T_{\mathrm{d,Si}} - T_{\mathrm{on,Si}} - T_{\mathrm{off,Si}})\,f_{\mathrm{s-Si}}. \tag{9}$$

Regarding the modeling of the switching loss of the Si-IGBT, the same methodology is applied as for SiC-MOS, which will not be reiterated here.

In summary, the total losses of the Si-IGBTs are

$$P_{\mathrm{Si-IGBT}} = P_{\mathrm{con,T}} + P_{\mathrm{con,D}} + P_{\mathrm{dead,D}} + P_{\mathrm{sw,Si}}. \tag{10}$$

D. Analytical Model of Copper Losses for Multiphase PMSMs

The motor's copper loss is primarily categorized into two parts: 1) one from the fundamental current and 2) the other from the harmonic current. Harmonic currents predominantly consist of low-order harmonics caused by the inverter's dead time and high-order harmonics due to inverter switching. The steady-state equivalent circuit of the motor is illustrated in Fig. 5 [36].

For multiphase motors with a sinusoidal distribution of windings, the counter EMF primarily comprises the fundamental component. Consequently, the solution for the harmonic current induced by harmonic voltages can be obtained using the superposition theorem. This implies that when solving for harmonic currents, the fundamental EMF can be set to zero when only harmonic voltages contribute to the generation of harmonic currents, thereby simplifying the solving process [37].

1) Copper Loss Due to the Fundamental Current: The copper loss produced by the fundamental current can be expressed as

$$P_{\mathrm{Cu1}} = \frac{m I_{\mathrm{pk}(1)}^2 R_{\mathrm{s}}}{2} + \frac{n I_{\mathrm{pk}(2)}^2 R_{\mathrm{s}}}{2}. \tag{11}$$

2) Copper Loss From the Low Harmonics of the Current Due to the Dead Time: The low harmonic voltage Δu_{s}, arising due to the presence of inverter dead time [38], can be expressed as

$$\Delta u_{\mathrm{s}} = -\mathrm{sign}\left(i_{\mathrm{s}}\right) \Delta U_{\mathrm{dc}} \tag{12}$$

where i_{s} stands for the phase current, and ΔU_{dc} can be given as

$$\Delta U_{\mathrm{dc}} = \frac{T_d}{T_s} U_{\mathrm{dc}}. \tag{13}$$

The voltage Δu_s can be decomposed into a series of harmonic components by the Fourier transform

$$\Delta u_{\mathrm{s}} = \Delta u_{\mathrm{s}(1)} + \sum_{h \in \mathrm{odd}, h \neq 1} u_{\mathrm{s}(h)} \tag{14}$$

with

$$u_{\mathrm{s}(h)} = U_h \cos\left(h\left(\omega t + \varphi_{(1)}\right)\right) \tag{15}$$

$$U_h = \frac{4 \Delta U_{\mathrm{dc}}}{\pi} \frac{(-1)^{\frac{h+1}{2}}}{h} \tag{16}$$

where $\Delta u_{\mathrm{s}(1)}$ represents the fundamental component of Δu_{s}, h denotes the harmonic order, odd signifies the set of odd numbers, and $\varphi_{(1)}$ is the phase angle of $\Delta u_{\mathrm{s}(1)}$.

Consequently, the amplitude of the lower harmonic current $I_{\mathrm{s}(h)}$ in each phase for multiphase PMSMs with sinusoidally distributed windings induced by the inverter dead time can be derived as

$$I_{\mathrm{s}(h)} = \frac{U_h}{|Z_h|} \tag{17}$$

with

$$Z_h = R_{\mathrm{s}} + jh\omega L_{\mathrm{s}}. \tag{18}$$

The copper losses resulting from the low harmonics of the current due to the dead time can be written as

$$P_{\mathrm{Cu2}} = \sum_{h \in \mathrm{odd}, h \neq 1} \frac{I_{\mathrm{s}(h)}^2 R_{\mathrm{s}}}{2}. \tag{19}$$

3) Copper Loss Due to the Harmonic Current Caused by PWM: In the case of double-edge naturally sampled PWM, the harmonic components of the PWM voltage waveform for each converter leg and the resulting phase voltage can be assessed through double Fourier integration [37], the harmonic components without common mode ones in star connection that are caused by the PWM can be expressed as

$$U_{\mathrm{s}(p\omega_c + q\omega_1)} = \sum_{p=1}^{+\infty} \sum_{q=-\infty}^{+\infty} A_{pq} \cos\left(p(\omega_c t + \theta_c) + q(\omega_1 t + \theta_1)\right) \tag{20}$$

with

$$A_{pq} = \begin{cases} \frac{2V_{\mathrm{dc}}}{p\pi} J_q\left(\frac{p\pi}{2} M\right) \sin\left(\frac{(p+q)\pi}{2}\right) & q = 3l \pm 1 \\ 0 & q = 3l \end{cases} \tag{21}$$

where $U_{\mathrm{s}\,(p\omega\,c + q\omega 1)}$ represents harmonic voltage components caused by PWM, l is an integer number, and ωc equals 2π times the switching frequency $f_{\text{s-SiC}}$ or $f_{\text{s-Si}}$.

The amplitude of the PWM harmonic current in each phase for multiphase motors with sinusoidally distributed windings can be derived as

$$I_{\mathrm{s}(p\omega_c + q\omega_1)} = \frac{U_{\mathrm{s}(p\omega_c + q\omega_1)}}{|Z_{p\omega_c + q\omega_1}|} \tag{22}$$

with

$$Z_{p\omega_c + q\omega_1} = R_{\mathrm{s}} + j(p\omega_c + q\omega_1) L_{\mathrm{s}}. \tag{23}$$

The copper losses induced by the PWM current harmonics can be represented as

$$P_{\mathrm{Cu3}} = \sum_{p=1}^{+\infty} \sum_{q=\pm 1}^{\pm\infty} \frac{{I_{\mathrm{s}(p\omega_c + q\omega_1)}}^2 R_{\mathrm{s}}}{2}. \tag{24}$$

In summary, the expression for overall copper losses can be defined as

$$\begin{aligned} P_{\mathrm{Cu}} = P_{\mathrm{Cu1}} &+ \sum_m \left(P_{\mathrm{Cu2}}(f_{\mathrm{s-SiC}}) + P_{\mathrm{Cu3}}(f_{\mathrm{s-SiC}})\right) \\ &+ \sum_n \left(P_{\mathrm{Cu2}}(f_{\mathrm{s-Si}}) + P_{\mathrm{Cu3}}(f_{\mathrm{s-Si}})\right). \end{aligned} \tag{25}$$

III. PROPOSED CONTROL STRATEGY AND EFFICIENCY ENHANCEMENT METHOD FOR TRACTION INVERTER WITH HYBRID SIC-MOS AND SI-IGBT BRIDGE ARMS

A. Basic FOC Control of Hybrid SiC-Si Traction Inverter and Multiphase PMSMs

For the multiphase motor system driven by a hybrid bridge arm structure inverter, due to the different parameters of the SiC-MOS bridge arm and Si-IGBT bridge arm devices. To realize the current control between the two sets of windings. The multithree phase control method can be used [39], [40].

The analysis in this work is performed on a six-phase motor with two neutral points. However, the methods presented can be extended to motors with more phases. In asymmetrical six-phase motors with two neutral points, the current of two sets of windings after the Clark transform is expressed as

$$\begin{cases} \boldsymbol{i}_{\alpha\beta}^{(1)} = \left[\mathbf{T}_3(0)\right] \boldsymbol{i}_{\mathrm{ABC}} \\ \boldsymbol{i}_{\alpha\beta}^{(2)} = \left[\mathbf{T}_3(\pi/6)\right] \boldsymbol{i}_{\mathrm{UVW}} \end{cases} \tag{26}$$

with

$$\left[\mathbf{T}_3(\gamma)\right] = \frac{2}{3} \begin{bmatrix} \cos(\gamma) & \cos\left(\gamma + \frac{2\pi}{3}\right) & \cos\left(\gamma + \frac{4\pi}{3}\right) \\ \sin\left(\gamma\right) & \sin\left(\gamma + \frac{2\pi}{3}\right) & \sin\left(\gamma + \frac{4\pi}{3}\right) \end{bmatrix} \tag{27}$$

$$\begin{gathered} \boldsymbol{i}_{\alpha\beta}^{(1)} = \begin{bmatrix} i_{\alpha 1} & i_{\beta 1} \end{bmatrix}^{\mathrm{T}}, \boldsymbol{i}_{\alpha\beta}^{(2)} = \begin{bmatrix} i_{\alpha 2} & i_{\beta 2} \end{bmatrix}^{\mathrm{T}} \\ \boldsymbol{i}_{\mathrm{ABC}} = \begin{bmatrix} i_{\mathrm{A}} & i_{\mathrm{B}} & i_{\mathrm{C}} \end{bmatrix}^{\mathrm{T}}, \boldsymbol{i}_{UVW} = \begin{bmatrix} i_{\mathrm{U}} & i_{\mathrm{V}} & i_{\mathrm{W}} \end{bmatrix}^{\mathrm{T}}. \end{gathered} \tag{28}$$

The current in the α_1-β_1 subspace after Park transformation is

$$\begin{cases} \boldsymbol{i}_{\mathrm{dq}}^{(1)} = \boldsymbol{P} \boldsymbol{i}_{\alpha\beta}^{(1)} \\ \boldsymbol{i}_{\mathrm{dq}}^{(2)} = \boldsymbol{P} \boldsymbol{i}_{\alpha\beta}^{(1)} \end{cases} \tag{29}$$

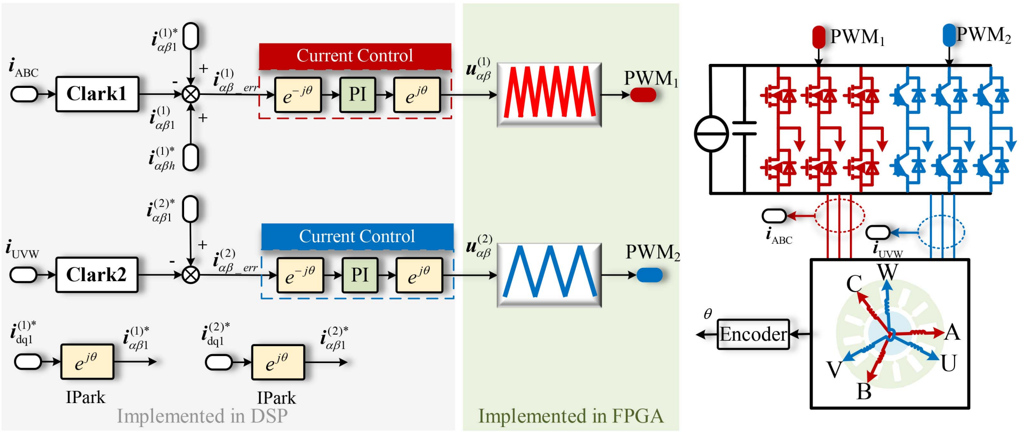

Fig. 6. Field-oriented control algorithm of multiphase PMSMs with hybrid bridge arms.

where

$$\boldsymbol{P} = \begin{bmatrix} \cos\theta & \sin\theta \\ -\sin\theta & \cos\theta \end{bmatrix}. \tag{30}$$

A block diagram of the field-oriented control for multiphase PMSMs driven by a hybrid bridge-arm structure inverter is shown in Fig. 6. This diagram shows the multi-dq control of two sets of three-phase windings independently [39]. The same control frequency is used for both sets of windings. The switching frequency of the SiC-MOS and Si-IGBT can be adjusted by varying the carrier frequency. In particular, this control architecture minimizes the control system delay [41], especially when operating at high control frequencies with low switching frequencies. Please note that the control frequency should be a whole number of multiples of the switching frequency.

The following methods, including torque ripple suppression, OSFC, and OLD strategy, are optimizations based on basic control. The torque ripple suppression method aims to reduce torque pulsation by injecting harmonic currents into the winding featuring the high-frequency SiC-MOS. The OSFC method calculates the optimal switching frequency of the Si-IGBT to enhance the system efficiency at the rated operating point based on the predetermined switching frequency of the SiC-MOS. The OLD problem focuses on optimizing the load sharing between the two sets of windings to improve the system efficiency under specified combinations of switching frequencies, particularly in the light load condition of the propulsion system.

B. *Selection for Switching Frequency of SiC-MOS Devices*

Increasing the switching frequency of SiC-MOS aims to enhance the system's control performance. Many metrics reflect the control performance of the system, such as torque ripple and speed pulsation.

This study focuses on minimizing the motor's torque ripple, with the lowest number of torque pulsations in an asymmetrical six-phase motor being 12 times the fundamental frequency [42].

The high switching frequency selection method employed in this article aims to effectively suppress the 12th harmonic torque pulsation. To enhance the control effectiveness of torque suppression, the switching frequency can be chosen to be several tens of times the 12th harmonic frequency [43]. Therefore, the minimum switching frequency $f_{\text{s-SiC-min}}$ of the SiC-MOS can be expressed, as shown in (31), where N_{num} represents the control cycles within the 12th harmonic frequency and f_1 is the fundamental frequency

$$f_{\text{s}-\text{SiC}-\text{min}} \geq N_{\text{num}} \cdot 12 f_1. \tag{31}$$

The SiC-MOS in this article employs a 20 kHz switching frequency as an example to enhance torque ripple suppression at $f_1 = 50$ Hz and $N_{\text{num}} = 33$.

The selection of high switching frequency in practice can be adjusted according to the requirements of control accuracy, but the control strategy proposed in this article is still applicable.

C. *Torque Ripple Suppression Method Utilizing High Switching Frequency SiC-MOS Bridge Arms*

Selecting a high switching frequency for the SiC-MOS bridge arm aims to enhance control performance by compensating for the coupled magnetic fields between motor phases. The high switching frequency allows the SiC-MOS bridge arm to compensate for the overall magnetic field, thereby suppressing the 12th torque ripple [42]. The following is a detailed analysis of the torque ripple suppression strategy.

The expression for the kth phase current containing each harmonic component is given by

$$i_k = \sum_h I_h \cos\left(h\left(\omega t - \alpha_k\right) + \varphi_h\right). \tag{32}$$

Similarly, the kth phase EMF expression containing each harmonic can be written as

$$e_k = \sum_v E_v \cos\left(v\left(\omega t - \alpha_k\right) + \psi_v\right). \tag{33}$$

This yields the expression for the motor torque as

$$T_e = \sum_{k=1}^{6} \frac{e_k i_k}{\omega_m} =$$

$$= \begin{cases} \frac{3E_vI_h}{\omega_m}\cos\left((h+v)\,\omega t+\varphi_h+\psi_v\right), h+v=12q \\ \frac{3E_vI_h}{\omega_m}\cos\left((h-v)\,\omega t+\varphi_h-\psi_v\right), h-v=12q \end{cases} \tag{34}$$

where q is the integer.

Therefore, the most dominant torque ripple in asymmetrical six-phase motors is 12th, and it mainly arises from the interaction of the fundamental EMF with the 11th and 13th harmonic currents, and the fundamental current with the 11th and 13th harmonic EMF [42], [44]. When control with $i_d = 0$ is used, assuming that the φ_1 and ψ_1 are equal to zero, the expression for the 12th torque ripple is

$$T_{12th} = \frac{3E_1I_{11}\cos(12\omega t+\varphi_{11})+3E_1I_{13}\cos(12\omega t+\varphi_{13})}{\omega_m} + \frac{3E_{11}I_1\cos(12\omega t+\psi_{11})+3E_{13}I_1\cos(12\omega t+\psi_{13})}{\omega_m}. \tag{35}$$

To reduce the 12th torque ripple to essentially zero, torque pulsation suppression can be achieved by injecting 11th or 13th harmonic currents. In our work, the 11th harmonic current is injected to suppress torque pulsation. The amplitude and phase of the injected 11th harmonic current are expressed as

$$\begin{cases} I_{11}^* = \frac{I_1\sqrt{E_{11}^2+E_{13}^2+2E_{11}E_{13}\cos(\psi_{11}-\psi_{13})}}{E_1} \\ \varphi_{11}^* = \pi + \arctan\left(\frac{E_{11}\cos\psi_{11}+E_{13}\cos\psi_{13}}{E_{11}\sin\psi_{11}+E_{13}\sin\psi_{13}}\right) \end{cases}. \tag{36}$$

It should be noted that the above amplitude refers to harmonics injected through all windings. If injected through only SiC-MOS set of windings, the injection amplitude must be doubled. Therefore, the expression for the injected 11th and 13th harmonic current in SiC-MOS set of wingdings is

$$\begin{cases} \boldsymbol{i}_{\mathrm{dq11}}^{(1)*} = \left[2I_{11}^*\cos\varphi_{11}^* \quad 2I_{11}^*\sin\varphi_{11}^*\right]^{\mathrm{T}} \\ \boldsymbol{i}_{\mathrm{dq13}}^{(1)*} = \left[0 \quad 0\right]^{\mathrm{T}} \end{cases}. \tag{37}$$

Note that to suppress torque pulsations, we only use SiC-MOS windings. The uncontrolled 11th and 13th harmonic currents are present in the motor winding where the low switching frequency Si-IGBT is located due to nonideal factors like inverter dead time, leading to torque pulsations. Therefore, we extract the 11th and 13th harmonics from the Si-IGBT winding and inject the opposite harmonics into the SiC-MOS located windings to compensate for the overall magnetic field of the motor and reduce the additional torque pulsations caused by the harmonic currents in the Si-IGBT located windings. Therefore, the final expression for the current references injected into the winding with SiC-MOS is given by

$$\begin{cases} \boldsymbol{i}_{\mathrm{dq11}}^{(1)*} = \left[2I_{11}^*\cos\varphi_{11}^* \quad 2I_{11}^*\sin\varphi_{11}^*\right]^{\mathrm{T}} - \boldsymbol{k}_{11}\boldsymbol{i}_{\mathrm{dq11}}^{(2)} \\ \boldsymbol{i}_{\mathrm{dq13}}^{(1)*} = -\boldsymbol{k}_{13}\boldsymbol{i}_{\mathrm{dq13}}^{(2)} \end{cases} \tag{38}$$

with

$$\boldsymbol{k}_{11} = \begin{bmatrix} k_{11}^1 & \\ & k_{11}^2 \end{bmatrix}, \boldsymbol{k}_{13} = \begin{bmatrix} k_{13}^1 & \\ & k_{13}^2 \end{bmatrix} \tag{39}$$

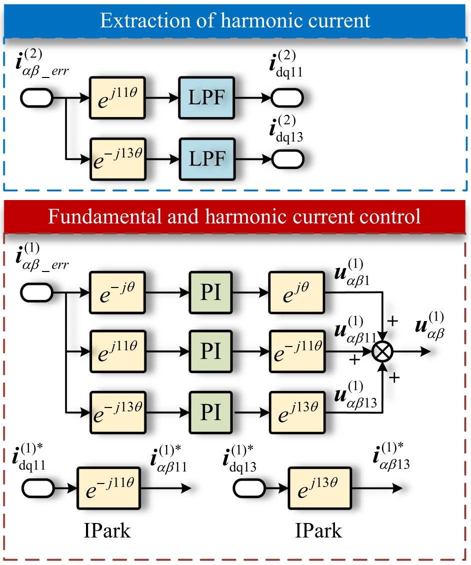

Fig. 7. Control block diagram of torque pulsation suppression section utilizing SiC-MOS bridge arms.

where $\boldsymbol{i}^{(2)}{}_{\mathrm{dq11}}$ and $\boldsymbol{i}^{(2)}{}_{\mathrm{dq13}}$ is the feedback 11th and 13th harmonic current in the second set of windings with Si-IGBT, the coefficient matrix $\boldsymbol{k}$ defaults to the unit matrix, which can be adjusted to improve the compensation as it compensates for the control delay [42].

The control block diagram considering torque pulsation suppression through the winding where the SiC-MOS is located is shown in Fig. 7, which consists of an extraction part to extract the current harmonics of the winding where the Si-IGBT bridge arm is located and a part to inject the harmonic current of the winding where the SiC-MOS is located in order to eliminate the 12th torque ripple. The current controller can be directly embedded and used in Fig. 6.

D. Proposed OSFC Method to Find Optimal Switching Frequency of Si-IGBT

The loss modeling method for multiphase motors and multiphase inverters with hybrid bridge arms is known from Section II, and the method concerning the switching frequency selection when high switching frequencies are used in the bridge arms of SiC-MOS devices is presented in Section III-B. Subsequently, the OSFC method will be elucidated for determining the switching frequency of the Si-IGBT to optimize system efficiency.

The OSFC problem can be mathematically described as

$$\begin{aligned} &\min P_{\mathrm{SiC\text{–}MOS}}(f_{\mathrm{s\text{–}SiC}})+P_{\mathrm{Si\text{–}IGBT}}(f_{\mathrm{s\text{–}Si}})+P_{\mathrm{Cu}}(f_{\mathrm{s\text{–}SiC}}, f_{\mathrm{s\text{–}Si}}) \\ &\text{s.t.} \\ &f_{\mathrm{s\text{–}SiC}} \geq f_{\mathrm{s\text{–}SiC\text{–}min}} \\ &f_{\mathrm{s\text{–}SiC}} \geq f_{\mathrm{s\text{–}Si}}. \end{aligned} \tag{40}$$

The OSFC problem aims to find the optimal switching frequency by minimizing losses in the inverter and motor while

TABLE I
KEY PARAMETERS OF TWO DEVICES

Parameter	Value	Parameter	Value
$R_{\mathrm{DS},on}$	50 mΩ	V_{CE0}	1.0 V
$R_{\mathrm{SD},on}$	50 mΩ	R_{CE}	29 mΩ
V_{BD}	4.9 V	V_{D}	1.2 V
R_{BD}	45 mΩ	R_{D}	15 mΩ
$T_{\mathrm{d,SiC}}$	1 μs	$T_{\mathrm{d,Si}}$	3 *us*
$T_{\mathrm{on,SiC}}$	31 ns	$T_{\mathrm{on,Si}}$	61 ns
$T_{\mathrm{off,SiC}}$	30 ns	$T_{\mathrm{off,Si}}$	600 ns
a_{SiC}	0.056 μJ/A^2	a_{Si}	0.293 μJ/A^2
b_{SiC}	1.213 μJ/A	b_{Si}	36.67 μJ/A
c_{SiC}	115.3 μJ	c_{Si}	251.23 μJ

TABLE II
KEY PARAMETERS OF SIX-PHASE MOTOR

Parameter	Value
Bus voltage	200 V
Rated power	2.3 kW
Rated speed	600 r/min
Rated torque	35 Nm
Rated current(RMS)	11 A
Rated voltage(peak)	90 V
Pole pairs	5
Stator phase resistance R_s	0.153 Ω
Stator phase inductance L_s	0.7 mH
Permanent magnet flux	0.15 Wb

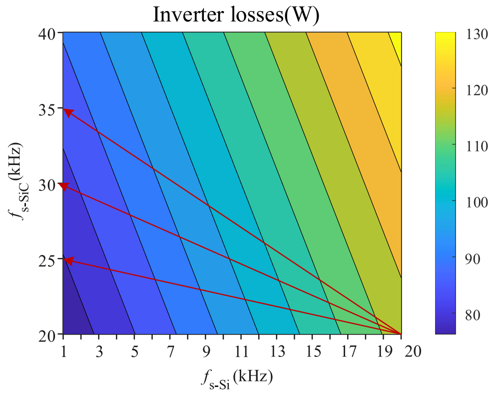

Fig. 8. Inverter losses with hybrid bridge legs.

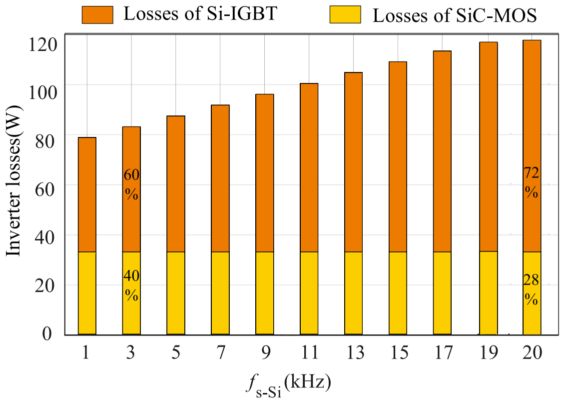

Fig. 9. Inverter losses and the share of losses of the SiC-MOS and the Si-IGBT bridge legs when the SiC-MOS operates at 20 kHz.

adhering to the minimum value of the selected SiC-MOS frequency, which is $f_{\text{s-SiC-min}}$, thereby determining the IGBT's switching frequency. The OSFC strategy primarily focuses on enhancing efficiency at the motor's rated torque point, which can be solved offline by scanning each combination of switching frequencies using MATLAB.

The OSFC method described above is universally applicable. In this work, we select C3M0040120J1(SiC-MOS) and IKW40N120T2(Si-IGBT) for analysis aimed at meeting the design requirements of inverters with a maximum bus voltage of 600 V and a peak phase current of 20 A. These devices share identical rated voltage and current capacities of 1200 V and 40 A. The 600 V bus voltage can be utilized for higher speed motors, expanding the inverter's application beyond low-speed and high-torque propulsion [22].

However, this article focuses on low-speed and high-torque multiphase PMSMs, which require a lower bus voltage. Considering the propulsion motor's demand, 200 V bus voltage suffices. Thus, simulations and experimental verifications in this article are conducted under a 200 V bus voltage.

The key parameters of both devices are displayed in Table I. These parameters were obtained through consultation of datasheets and fitting. Parameters a, b, and c represent the fitted switching loss parameters at a junction temperature of 100 °C, an external driving resistance of 10 Ω, and a bus voltage of 200 V, respectively.

The parameters of the six-phase motor are shown in the Table II.

In the OSFC problem, Fig. 8 illustrates the results of considering only the inverter losses. The red line in Fig. 8 demonstrates that inverter losses decrease as the switching frequency of the SiC-MOS increases and that of the Si-IGBT decreases. The breakdown of the losses for both Si-MOS and Si-IGBT is presented in Fig. 9 with SiC-MOS operating at 20 kHz, it can be seen that reducing the switching frequency of Si-IGBT has a significant effect on reducing the converter losses.

However, solely concentrating on inverter losses inadequately addresses the OSFC problem, as it entails continuously reducing the switching frequency of the Si-IGBT, leading to increased motor harmonic copper losses. Therefore, motor harmonic copper losses must be considered concurrently. The copper loss of the motor is shown in Fig. 10 when different switching frequency combinations are adopted.

The analytical results, including both inverter losses and motor copper losses, are depicted in Fig. 11. In solving the OSFC problem, when the $f_{\text{s-SiC}}$ constraint (31) is enforced, optimal system efficiency is achieved by appropriately reducing the switching frequency of the Si-IGBT. Given that the $f_{\text{s-SiC}}$ in this work must be greater than or equal to 20 kHz in Section III-B, theoretical analysis indicates that the optimal switching frequency for $f_{\text{s-Si}}$ is 3 kHz, minimizing system losses.

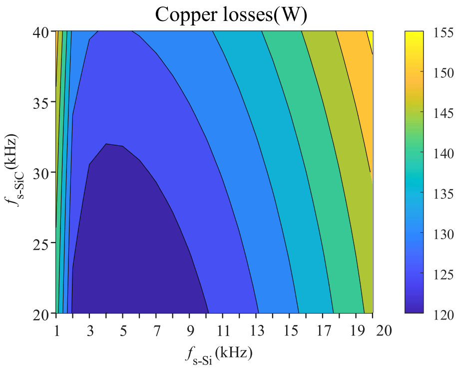

Fig. 10. Copper losses of the motor driven by inverter with hybrid bridge legs.

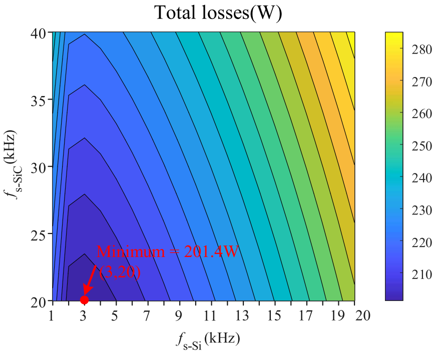

Fig. 11. Theoretical system losses with different switching frequency combinations.

E. Proposed OLD Strategy for Light-Load Efficiency Improvement

Fig. 9 shows that the losses in the Si IGBT bridge arm are a larger proportion of the total inverter losses. Despite the identical rated current capacity of each phase in the hybrid bridge arm inverter, there are still degrees of freedom to optimize the load distribution between the windings driven by SiC-MOS and Si-IGBT bridge arms under light loads, thus, further enhancing system efficiency.

Notably, the proposed OLD strategy is analyzed with the determined optimal switching frequency combination. In this study, the switching frequency combination solved by OSFC method with 20 kHz for the SiC-MOS and 3 kHz for the Si-IGBT is adopted. The demand for solving the OLD problem lies in determining the optimal distribution of the load between the two sets of windings. The sum of the loads of the two sets of windings should be equal to the total load of the motor

$$\boldsymbol{i}_{\alpha\beta} = \boldsymbol{i}_{\alpha\beta}^{(1)} + \boldsymbol{i}_{\alpha\beta}^{(2)}. \tag{41}$$

Hence, the load on the two sets of windings can be expressed as

$$\begin{cases} \boldsymbol{i}_{\alpha\beta}^{(1)} = d\boldsymbol{i}_{\alpha\beta} \\ \boldsymbol{i}_{\alpha\beta}^{(2)} = (1-d)\boldsymbol{i}_{\alpha\beta} \end{cases}. \tag{42}$$

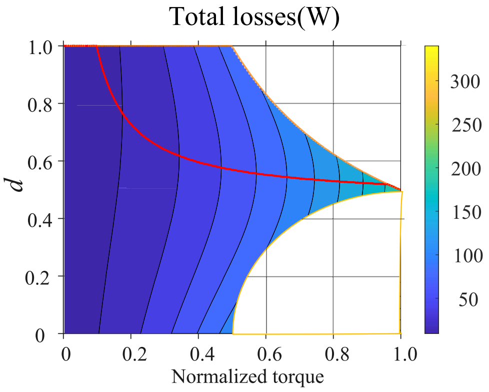

Fig. 12. Optimal distribution line from no load to rated torque.

It also follows from (26) that

$$\begin{cases} \boldsymbol{i}_{\alpha\beta}^{(1)} = I_{\text{pk}(1)} e^{j(\omega t + \sigma_1)} \\ \boldsymbol{i}_{\alpha\beta}^{(2)} = I_{\text{pk}(2)} e^{j(\omega t + \sigma_1)} \end{cases} \tag{43}$$

where the I_{pkmax} is the maximum phase current limit, σ_1 is the initial phase angle of the current vector.

Therefore, at a certain load level, the OLD problem can be described as (44), which aims to solve the current distribution coefficient d to minimize system losses. The OLD problem is solved by simply scanning the losses in MATLAB offline at different load levels under different current distribution ratios, and a curve for the optimal distribution ratio d can be obtained.

The OLD line is determined by (44) across various load levels from no load to rated load with specified speed, as depicted in Fig. 12. It reveals that under light load conditions, the SiC-MOS is favored to handle the load, aiming to enhance system efficiency

$$\begin{aligned} &\min \quad P_{\text{SiC-MOS}}(d) + P_{\text{Si-IGBT}}(d) + P_{\text{Cu}}(d) \\ &\text{s.t.} \\ &\left|\boldsymbol{i}_{\alpha\beta}^{(1)}\right| \le I_{\text{pkmax}} \\ &\left|\boldsymbol{i}_{\alpha\beta}^{(2)}\right| \le I_{\text{pkmax}} \\ &\boldsymbol{i}_{\alpha\beta}^{(1)} = d\boldsymbol{i}_{\alpha\beta} \\ &\boldsymbol{i}_{\alpha\beta}^{(2)} = (1-d)\boldsymbol{i}_{\alpha\beta} \\ &d \in [0,1]. \end{aligned} \tag{44}$$

A comparison of losses using the proposed OLD strategy and with traditional even distribution is illustrated in Fig. 13. It can be observed that at light load, the total loss reduction reaches up to 12% when optimal allocation is employed, as opposed to even distribution. The percentage of loss reduction is defined as

$$\xi = \frac{P_{\text{even-dis}} - P_{\text{optimal-dis}}}{P_{\text{even-dis}}} \tag{45}$$

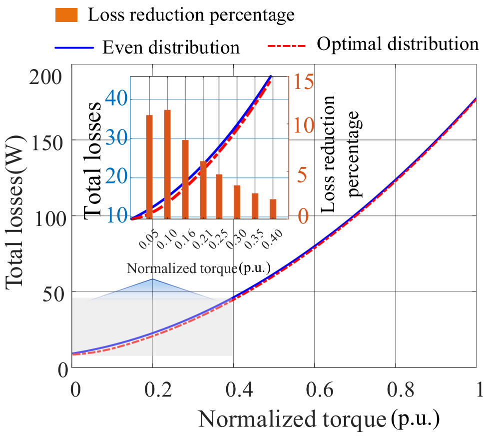

Fig. 13. Losses when loads are evenly distributed compared to the proposed OLD strategy in light-load conditions.

TABLE III
COST BREAKDOWN OF THE INVERTER WITH HYBRID BRIDGE ARMS AND FULL SIC-MOS SOLUTION FOR SIX-PHASE MOTOR DRIVE

Inverter with hybrid bridge arms	Cost and Number	Inverter with full SiC-MOS	Cost and Number
C3M0040120J1	31USD*6	C3M0040120J1	31USD*12
IKW40N120T2	9USD*6	×	×
2SD315AI (IGBT Driver)	100USD*3	×	×
62EM1 (SiC-MOS Driver)	330USD*3	62EM1 (SiC-MOS Driver)	330USD*6
Total Cost	1530USD	Total Cost	2352USD

where $P_{\text{even-dis}}$ is the total losses when the load is evenly distributed, and $P_{\text{optimal-dis}}$ is the total losses when the OLD is used.

Due to the substantial proportion of losses experienced under light loads, a 12% reduction in losses holds significant importance in enhancing the efficiency of the system during such conditions.

It should be noted that because the loss of the converter and motor cannot be completely accurate, some errors are inevitable. However, the results can still serve as a useful reference for actual operation. We can fine-tune near the optimal value obtained offline to quickly obtain the optimal switching frequency combination and OLD in practice.

F. Comparison With All Si-IGBT and All SiC-MOS Solutions

The primary benefit of utilizing an inverter with hybrid bridge arms over an all-SiC-MOS inverter is cost-saving. The cost analysis comparing the hybrid bridge arm solution with full SiC-MOS, utilizing the C3M0040120J1 and IKW40N120T2 devices as examples, is presented in Table III. Prices were sourced from Mouser.cn. The comparison primarily focuses on the devices and the driver circuit, revealing that the hybrid bridge arm solution can achieve a cost reduction of 35%.

The main advantage of utilizing an inverter with a hybrid bridge arm over an all-Si-IGBT inverter is the reduction in losses. As depicted in Fig. 14, utilizing hybrid bridge arms can result in 28% loss reductions compared to a full Si-IGBT solution in rated points. The utilization of SiC-MOS bridge arms constitutes one of the primary factors contributing to loss reduction, with additional reductions achieved through the implementation of OSFC and OLD strategies for the hybrid bridge arms.

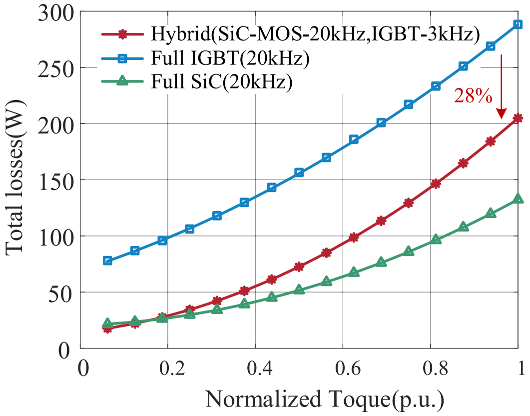

Fig. 14. Comparison with all Si-IGBT(20 kHz) and all SiC-MOS(20 kHz) solutions.

Compared to the all-Si-IGBT scheme, the proposed hybrid bridge arm can effectively suppress the 12th torque ripple through the increase in switching frequency of SiC-MOS, ensuring enhanced control performance. And the efficiency of the system can be further enhanced through the utilization of OSFC and OLD methods. Furthermore, in comparison to all SiC-MOS solutions, the proposed hybrid bridge arm structure offers substantial cost savings.

IV. EXPERIMENTAL RESULTS

A. Experimental Setup

The experiments were performed on a six-phase permanent magnet synchronous motor (PMSM) with two isolated neutral points. The motor parameters are detailed in Table II. Additionally, the main circuit of the inverter with a hybrid bridge arm structure is illustrated in Fig. 15 with exploded view and prototype.

The inverter is controlled using a DSP and FPGA framework, where the DSP is responsible for closed-loop control and generating the duty cycle, while the FPGA is tasked with modulating and generating the switching signals, as shown in Fig. 16. In the hybrid switching frequency scheme, the control frequency for both sets of three-phase windings is identical. In this study, the control frequency is set to 20 kHz, as the switching frequency of SiC-MOS is chosen as 20 kHz. The distinction lies in the fact that the FPGA employs a different switching frequency. It should be noted that in this control architecture, when the control frequency is 20 kHz, it is an integer multiple of the switching frequency. Therefore, the switching frequency of the Si-IGBT can be selected as 20 kHz, 10 kHz, 6.6 kHz, 5 kHz, 4 kHz, 3.3 kHz, 2 kHz, or 1 kHz. Hence, based on theoretical analysis, the optimal switching frequency of the IGBT is determined to be 3 kHz, which should be selected as 3.3 kHz in the experiment.

In the overall efficiency test of the propulsion system, the input power of the system is measured by the power analyzer,

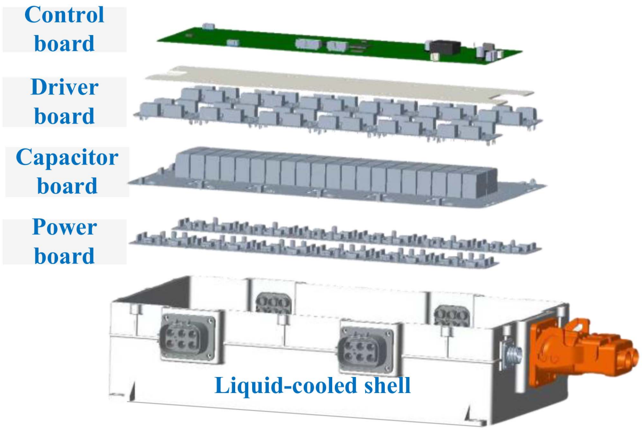

(a)

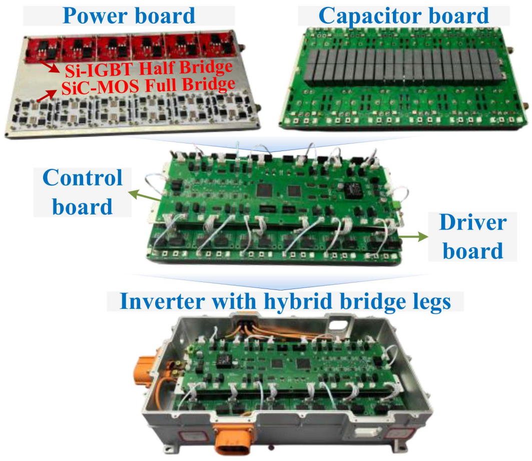

(b)

Fig. 15. Inverter with hybrid bridge legs. (a) Exploded view of the overall structure. (b) Inverter board structure in practice.

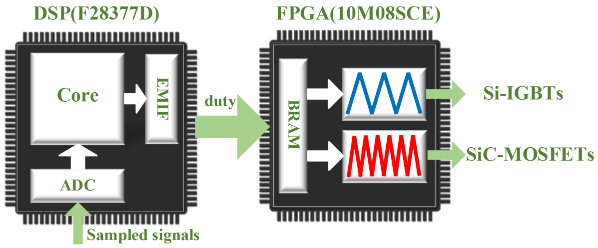

Fig. 16. Control framework in the DSP and FPGA.

which is Zimmer LMG670 on the dc source side, while the output power is measured by the torque and speed meter, which is Kistler 4502, as shown in Fig. 17. The output power P_{out} can be derived as

$$P_{\text{out}} = \frac{1}{D}\int_D T\omega \tag{46}$$

where T and ω are the output torque and angular velocity measured by torque and speed meter, and D is the integration

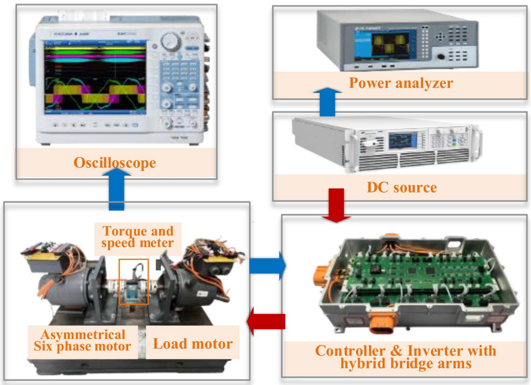

Fig. 17. Experimental platform.

time, which can be chosen as a multiple of the fundamental period.

Therefore, the total losses of the propulsion system are calculated by subtracting the input power from the output power as

$$P_{\text{loss}} = P_{\text{in}} - P_{\text{out}} \tag{47}$$

where P_{in} is measured by power analyzer and P_{out} by torque and speed meter, and P_{loss} is the total losses of the propulsion system.

It is worth noting that P_{loss} encompasses all losses in the propulsion system, comprising inverter losses, copper and iron losses, eddy current losses, mechanical losses, and any additional losses occurring in the motor. In contrast, the analyses in Section III only considered the most significant inverter losses and the motor's copper losses. Therefore, there are some differences between them. However, since the optimization objective of this study is to minimize the overall losses of the system, the correctness of the proposed method can be verified based on P_{loss}.

B. Experimental Validation of 12th Torque Ripple Suppression Method Utilizing High Switching Frequency SiC-MOS Bridge Arms

To validate the effectiveness of 12th torque pulsation suppression, experiments are conducted at different loads and torque. The torque ripple suppression method utilizing high switching frequency SiC-MOS bridge arms is described in Section III-C. Torque measurements are obtained using the Kistler 4502 torque meter. The E_{11}/E_1 and E_{13}/E_1 of the motor are 0.01 and 0.05, respectively, and ψ_{11} and ψ_{13} are π and 0.

Fig. 18 presents the results of implementing the torque ripple suppression algorithm at rated torque and rated motor speed using an inverter with a hybrid bridge-arm structure. The switching frequencies utilized are 20 kHz for SiC-MOS and 3.3 kHz for Si-IGBT. The FFT analysis of the torque, as shown in Fig. 19, indicates that the amplitude of the 12th torque ripple decreases from 1.3 Nm to 0.74 Nm, representing a 43% reduction. This

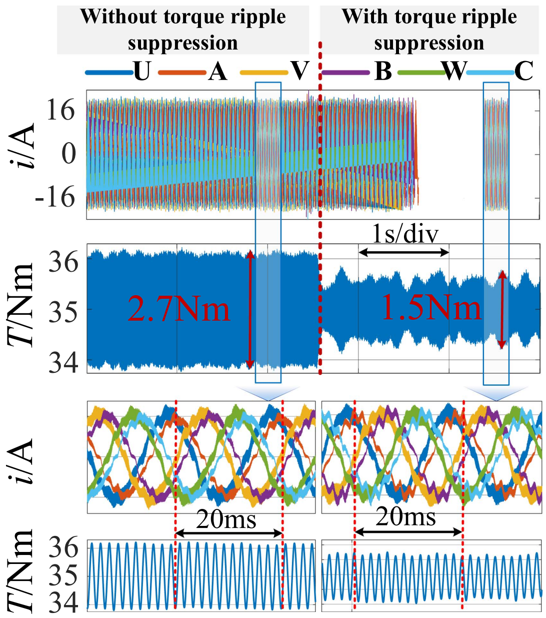

Fig. 18. Current and torque waveforms before and after applying torque ripple suppression at steady state at 600 r/min and rated torque 35 Nm with hybrid arms inverter.

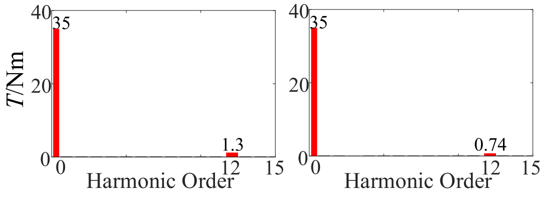

(a) (b)

Fig. 19. FFT analysis of the torque at 600 r/min and rated torque. (a) Without torque ripple suppression. (b) With torque ripple suppression.

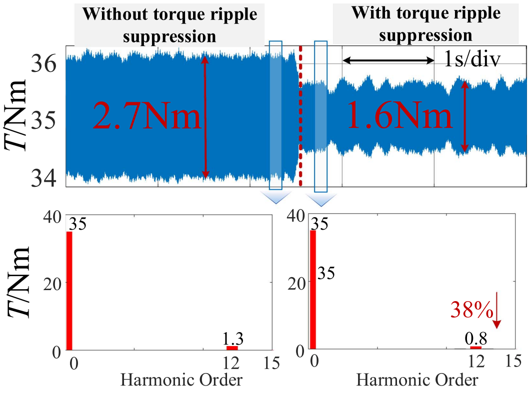

Fig. 20. Torque waveforms and FFT analysis before and after applying torque ripple suppression at steady state at 300 r/min and the rated torque.

reduction highlights the effectiveness of the suppression algorithm. Additionally, Fig. 18 provides current waveforms before and after the implementation of the torque ripple suppression algorithm. It is observed that harmonic currents are injected into the set of windings where the SiC-MOS is located to suppress torque ripples.

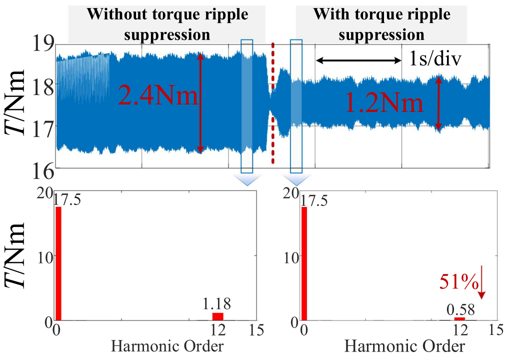

Fig. 21. Torque waveforms and FFT analysis before and after applying torque ripple suppression at steady state at 600 r/min and half of the rated torque.

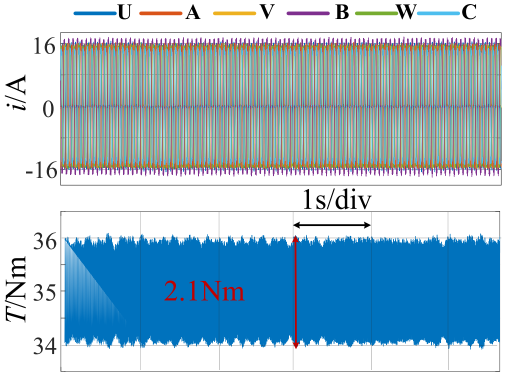

Fig. 22. Current and torque waveforms at steady state at 600 r/min and rated torque 35 Nm with full-IGBT inverter operating at 20 kHz.

The effectiveness of the torque ripple suppression strategy at different speeds and loads is shown in Figs. 20 and 21. It can be seen that the proposed torque ripple suppression method can effectively suppress torque pulsation at different speeds and loads.

When utilizing the full Si-IGBT inverter with a switching frequency of 20 kHz, the current and torque waveforms of each phase of the motor at rated torque and speed are depicted in Fig. 22, with torque ripple measured at 2.1 Nm. Comparatively, when employing the hybrid bridge arm structure, with SiC-MOS operating at 20 kHz and IGBT at 3.3 kHz, torque control performance can match that of the full IGBT at 20 kHz when utilizing the torque pulsation compensation algorithm. Therefore, it is feasible to ensure overall torque control by elevating the SiC-MOS switching frequency while concurrently reducing the switching frequency of Si-IGBT.

C. *Experimental Validation of the OSFC Methodology*

The feasibility of increasing the switching frequency of the SiC-MOS to suppress torque ripple and ensure overall control performance has been validated in Section IV-B.

The following presents experimental verification of the proposed OSFC strategy, aiming to optimize system efficiency by decreasing the switching frequency of the Si-IGBT while maintaining the control performance ensured by a SiC-MOS

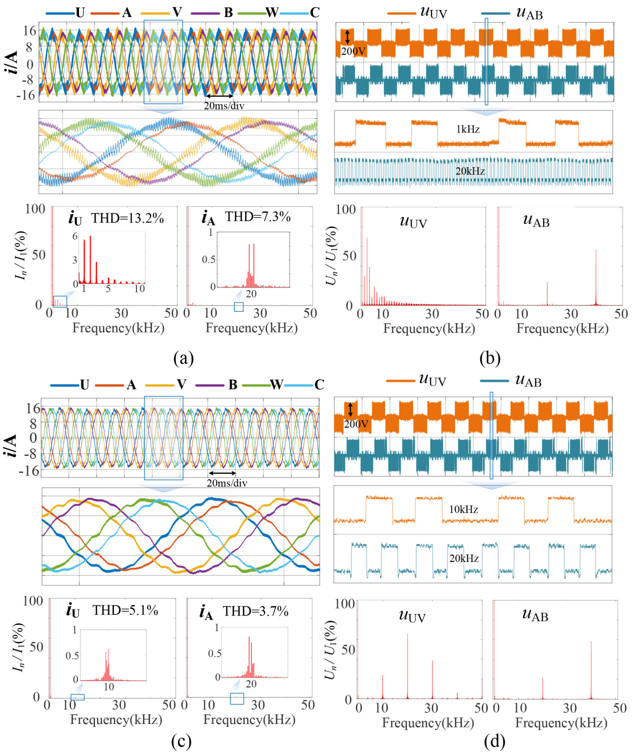

Fig. 23. Waveforms and FFT analysis of voltage and current in the hybrid bridge-arm inverter at rated motor load and rated speed. (a) and (b) Switching frequency of 20 kHz for the SiC-MOS and 1 kHz for the Si-IGBT. (c) and (d) Switching frequency of 20 kHz for SiC-MOS and 10 kHz for Si-IGBT.

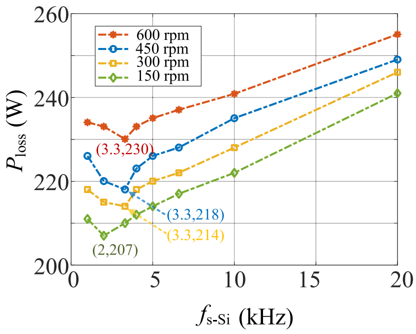

Fig. 24. System losses of Si-IGBT with different switching frequencies at SiC-MOS operating at 20 kHz with different speed at rated torque.

TABLE IV
COMPARISON OF THEORETICAL AND EXPERIMENTAL OSFC AT DIFFERENT SPEEDS

Speed (rpm)	Theoretical optimal combination ($f_{s\text{-Si}}$, $f_{s\text{-SiC}}$)	Experimental optimal combination ($f_{s\text{-Si}}$, $f_{s\text{-SiC}}$)
600	(3 kHz, 20 kHz)	(3.3 kHz, 20 kHz)
450	(3 kHz, 20 kHz)	(3.3 kHz, 20 kHz)
300	(3 kHz, 20 kHz)	(3.3 kHz, 20 kHz)
150	(3 kHz, 20 kHz)	(2 kHz, 20 kHz)

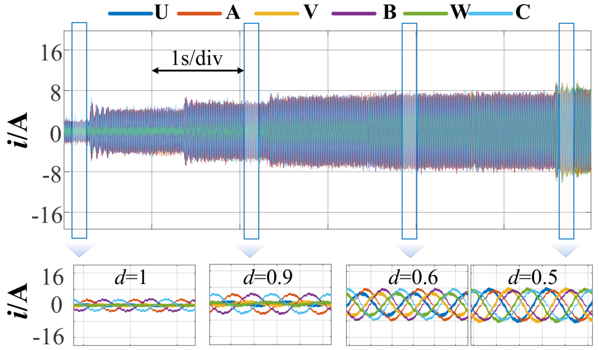

Fig. 25. Current waveforms at rated speed and 0–0.4 times the rated torque with OLD problem.

switching frequency of 20 kHz. Fig. 23 illustrates the waveforms and FFT analysis of phase current and line voltage under different switching frequency combinations at the rated speed and torque of the motor. It is observed that reducing the Si-IGBT switching frequency leads to a decrease in inverter losses, but this reduction is accompanied by an increase in harmonic currents, which will generate copper loss. Therefore, a tradeoff process exists to determine the optimal Si-IGBT switching frequency for maximizing system efficiency.

The losses of the system with different speeds when the switching frequency of the Si-IGBT is 20 kHz, 10 kHz, 6.6 kHz, 5 kHz, 4 kHz, 3.3 kHz, 2 kHz, or 1 kHz and the switching frequency of the SiC-MOS is 20 kHz are given in Fig. 24, and it can be seen that the reduction of the switching frequency of the Si-IGBT is of great importance in improving the efficiency of the system. Experimental results reveal the optimal switching frequency for Si-IGBT at different speeds, demonstrating a close alignment between the theoretical and actual values, as shown in Table IV. A slight deviation exists at 150 r/min, but the difference in loss is not significant. Therefore, the proposed OSFC strategy is effective at different speeds.

D. Experimental Validation of the OLD Strategy

The following is an experimental verification of the OLD problem. The optimal current distribution factor d is calculated and prestored in the microcontroller.

The current waveforms at various loads with OLD are depicted in Fig. 25, showcasing motor speeds of 600 r/min and load levels ranging from 0–0.4 times rated torque. Notably, differences in current magnitude between the two sets of windings are observed with varying load current distribution factor d.

Additionally, Fig. 26 illustrates the total loss of the propulsion system measured during experiments operating at load levels ranging from 0–0.4 times the rated torque at different speeds. Employing OLD leads to a reduction in system loss of up to 15% at load levels ranging from 0 to 0.1 times the rated load with different speeds. Given the inherently low efficiency of the system at light loads, reducing losses by 15% can lead to a corresponding increase in system efficiency by approximately 2-3%.

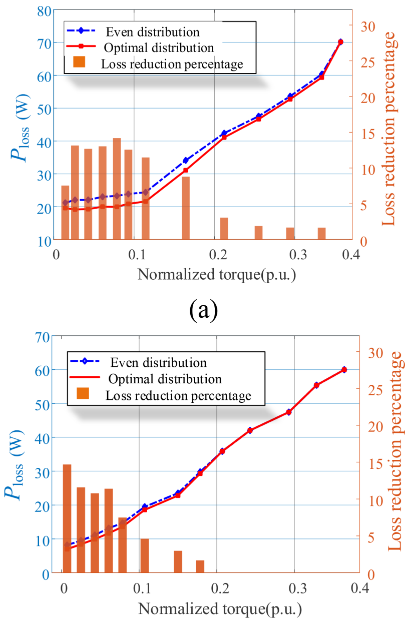

(a)

(b)

Fig. 26. Total Losses Loss reduction in the light load at 0–0.4 rated torque with proposed OLD method compared to even distribution. (a) 600 r/min. (b) 300 r/min.

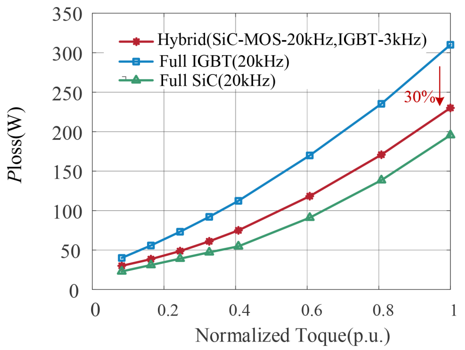

Fig. 27. System overall losses compared with full-SiC and full-IGBT.

E. Loss Comparison With All-SiC-MOS and All-Si-IGBT Scheme

In the experimental test shown in Fig. 27, the hybrid bridge-arm inverter incorporating OSFC and OLD strategies is compared with the all-Si-IGBT scheme. It is observed that at rated load, the hybrid bridge-arm inverter can reduce losses by 30%, a substantial improvement in system efficiency.

The hybrid bridge-arm structure employed not only reduces costs by 35% compared to an all-SiC-MOS solution but also diminishes system losses by 30% compared to an all-Si-IGBT (20 kHz) setup. Furthermore, the hybrid bridge-arm solution demonstrates comparable torque control performance to that of an all-Si-IGBT with 20 kHz configuration by the proposed torque pulsation suppression method as shown previously in Figs. 18 and 22.

V. CONCLUSION

This article proposes a hybrid inverter structure with bridge legs of SiC-MOS and Si-IGBT devices to fully exploit the advantages of low switching losses of SiC-MOS. Elevating the switching frequency of SiC-MOS and implementing the proposed torque ripple suppression method can result in effective mitigation of torque pulsations and enhancement of control performance. Building upon this foundation, the proposed OSFC method optimizes system efficiency by lowering the switching frequency of Si-IGBT. Furthermore, the efficiency of the ship propulsion system at light loads is further enhanced by the proposed OLD method. These methods have been experimentally validated, confirming that the torque ripple suppression method can effectively reduce pulsation by over 43%. Additionally, the correctness of the OSFC method is established, and the proposed OLD method demonstrates a potential reduction of up to 15% in propulsion system losses under light load conditions. Finally, the efficiency of the hybrid bridge-arm scheme is compared with that of the all-Si-IGBT scheme, revealing a potential reduction of up to 30% in system losses while saving 35% cost compared to all SiC-MOS inverters.

REFERENCES

[1] E. Levi, R. Bojoi, F. Profumo, H. A. Toliyat, and S. Williamson, "Multiphase induction motor drives - a technology status review," *IET Electr. Power Appl.*, vol. 1, no. 4, pp. 489–516, Jul. 2007.

[2] S. S. Williamson, A. K. Rathore, and F. Musavi, "Industrial electronics for electric transportation: Current State-of-the-art and future challenges," *IEEE Trans. Ind. Electron.*, vol. 62, no. 5, pp. 3021–3032, May 2015.

[3] A. Lega, M. Mengoni, G. Serra, A. Tani, and L. Zarri, "Space vector modulation for multiphase inverters based on a Space partitioning algorithm," *IEEE Trans. Ind. Electron.*, vol. 56, no. 10, pp. 4119–4131, Oct. 2009.

[4] E. Levi, "Advances in converter control and innovative exploitation of additional degrees of freedom for multiphase machines," *IEEE Trans. Ind. Electron.*, vol. 63, no. 1, pp. 433–448, Jan. 2016.

[5] J. M. Apsley et al., "Propulsion drive models for full electric marine Propulsion systems," *IEEE Trans. Ind. Appl.*, vol. 45, no. 2, pp. 676–684, Mar./Apr. 2009.

[6] Z. R. Zhang, H. H. Guo, Y. C. Liu, Q. F. Zhang, P. L. Zhu, and R. Iqbal, "An improved sensorless control strategy of ship IPMSM at full speed range," *IEEE Access*, vol. 7, pp. 178652–178661, 2019.

[7] N. Oswald, P. Anthony, N. McNeill, and B. H. Stark, "An experimental investigation of the tradeoff between switching losses and EMI generation with hard-switched all-Si, Si-SiC, and all-SiC device combinations," *IEEE Trans. Power Electron.*, vol. 29, no. 5, pp. 2393–2407, May 2014.

[8] A. K. Morya et al., "Wide bandgap devices in AC electric drives: Opportunities and challenges," *IEEE Trans. Transp. Electrific.*, vol. 5, no. 1, pp. 3–20, Mar. 2019.

[9] K. Shirabe et al., "Advantages of high frequency PWM in AC motor drive applications," in *Proc. IEEE Energy Convers. Congr. Expo.*, 2012, pp. 2977–2984.

[10] T. F. Zhao, J. Wang, A. Q. Huang, and A. Agarwal, "Comparisons of SiC MOSFET and Si IGBT based motor drive systems," in *Proc. IEEE Ind. Appl. Annu. Meeting*, 2007, pp. 331–335.

[11] W. Taha, A. Jinesh, and A. Emadi, "On the feasibility of SiC-based multiphase traction inverters for EV applications: A case study," in *Proc. 48th Annu. Conf. IEEE Ind. Electron. Soc.*, 2022, pp. 1–6.

[12] D. Zhang, J. B. He, and D. Pan, "A megawatt-scale medium-voltage high-efficiency high power density 'SiC plus Si' hybrid three-level ANPC inverter for aircraft hybrid-electric propulsion systems," *IEEE Trans. Ind. Appl.*, vol. 55, no. 6, pp. 5971–5980, Nov./Dec. 2019.

[13] D. Woldegiorgis, W. Yuheng, W. Yuqi, and H. A. Mantooth, "A high efficiency and low cost ANPC inverter using hybrid Si/SiC switches," *IEEE Open J. Ind. Appl.*, vol. 2, pp. 154–167, Jun. 2021.

[14] P. D. Judge and S. Finney, “2-Level Si IGBT converter with parallel part-rated SiC converter providing partial power transfer and active filtering,” in *Proc. 20th Workshop Control Model. Power Electron.*, 2019, pp. 1–7.

[15] Q. X. Guan et al., “An extremely high efficient three-level active neutral-point-clamped converter comprising SiC and Si hybrid power stages,” *IEEE Trans. Power Electron.*, vol. 33, no. 10, pp. 8341–8352, Oct. 2018.

[16] N. Li, M. B. Macavilca, C. Q. Wu, S. Finney, and P. D. Judge, “Converter topology for megawatt scale applications with reduced filtering requirements, formed of IGBT bridge operating in the 1000 hz region with parallel part-rated high-frequency SiC MOSFET bridge,” *IEEE Trans. Power Electron.*, vol. 39, no. 1, pp. 799–813, Jan. 2024.

[17] D. Zhang and X. She, “Hybrid multilevel converter with silicon and silicon carbide devices: Impact to aviation industry and beyond,” *IEEE Trans. Power Electron.*, vol. 38, no. 6, pp. 6806–6810, Jun. 2023.

[18] S. Ni, L. Peng, and Z. Zheng, “Switching frequency optimization method and control strategy of propulsion inverter for multiphase motors with hybrid SiC-MOS and Si-IGBT bridge legs,” in *Proc. 26th Int. Conf. Elect. Mach. Syst.*, 2023, pp. 2931–2937.

[19] F. Acosta-Cambranis, J. Zaragoza, L. Romeral, and N. Berbel, “Comparative analysis of SVM techniques for a five-phase VSI based on SiC devices,” *Energies*, vol. 13, no. 24, Dec. 2020, Art. no. 6581.

[20] I. Vasile et al., “Electric drives with multiphase motors as a better solution for traction systems,” in *Proc. 11th Int. Symp. Adv. Topics Electr. Eng.*, 2019, pp. 1–5.

[21] J. J. Zhu, J. X. Yuan, Z. L. Nie, J. Xu, and X. Zeng, “Research on dual 12-phase 12-slot winding permanent-magnet propulsion system based on all-SiC power module,” *IEEE Trans. Ind. Appl.*, vol. 58, no. 6, pp. 7692–7700, Nov. 2022.

[22] P. Zhou, Y. L. Xu, and F. Xin, “Study of magneto-thermal problems in low-speed high-torque direct drive PMSM based on demagnetization detection and loss optimization of permanent magnets,” *IEEE Access*, vol. 11, pp. 92055–92069, 2023.

[23] A. Acquaviva, A. Rodionov, A. Kersten, T. Thiringer, and Y. J. Liu, “Analytical conduction loss calculation of a MOSFET three-phase inverter accounting for the reverse conduction and the blanking time,” *IEEE Trans. Ind. Electron.*, vol. 68, no. 8, pp. 6682–6691, Aug. 2021.

[24] S. Belkhode, A. Shukla, and S. Doolla, “A highly efficient Si-/SiC-based hybrid active NPC converter with a novel modulation scheme,” *IEEE Trans. Ind. Appl.*, vol. 58, no. 6, pp. 7445–7456, Nov. 2022.

[25] V. Ruuskanen, J. Nerg, M. Rilla, and J. Pyrhönen, “Iron loss analysis of the permanent-magnet synchronous machine based on finite-element analysis over the electrical vehicle drive cycle,” *IEEE Trans. Ind. Electron.*, vol. 63, no. 7, pp. 4129–4136, Jul. 2016.

[26] K. Fujisaki, M. Sakai, S. Takeda, and I. I. A. Soc, “Motor loss increment of induction Motor driven by PWM inverter in comparison with inverter circuit loss,” in *Proc. 15th Int. Conf. Elect. Mach. Syst.*, 2012, pp. 1–6.

[27] S. Wu, Z. Li, and W. Tong, “Research on thermal calculation and end winding heat conduction optimization of low speed high torque permanent magnet synchronous motor,” *CES Trans. Electr. Mach. Syst.*, vol. 7, no. 4, pp. 397–403, Dec. 2023.

[28] D. Christen and J. Biela, “Analytical switching loss modeling based on datasheet parameters for MOSFETs in a half-bridge,” *IEEE Trans. Power Electron.*, vol. 34, no. 4, pp. 3700–3710, Apr. 2019.

[29] S. Yin, Y. T. Liu, Y. Liu, K. J. Tseng, J. Pou, and R. Simanjorang, “Comparison of SiC voltage source inverters using synchronous rectification and freewheeling diode,” *IEEE Trans. Ind. Electron.*, vol. 65, no. 2, pp. 1051–1061, Feb. 2018.

[30] H. Liu, H. Wu, Y. Lu, and Y. Xing, “A high efficiency inverter based on SiC MOSFET without externally anti-paralleled diodes,” in *Proc. IEEE Appl. Power Electron. Conf. Expo.*, Mar. 2014, pp. 163–167.

[31] Z. Y. Zhang, F. Wang, L. M. Tolbert, B. J. Blalock, and D. J. Costinett, “Evaluation of switching performance of SiC devices in PWM inverter-fed induction motor drives,” *IEEE Trans. Power Electron.*, vol. 30, no. 10, pp. 5701–5711, Oct. 2015.

[32] X. D. Wang, Z. M. Zhao, K. Li, Y. C. Zhu, and K. N. Chen, “Analytical methodology for loss calculation of SiC MOSFETs,” *IEEE J. Emerg. Sel. Topics Power Electron.*, vol. 7, no. 1, pp. 71–83, Mar. 2019.

[33] A. K. Sadigh, V. Dargahi, and K. A. Corzine, “Analytical determination of conduction and switching power losses in flying-capacitor-based active neutral-point-clamped multilevel converter,” *IEEE Trans. Power Electron.*, vol. 31, no. 8, pp. 5473–5494, Aug. 2016.

[34] A. Negahdari, A. G. Yepes, J. Doval-Gandoy, and H. A. Toliyat, “Efficiency enhancement of multiphase electric drives at light-load operation considering both converter and stator copper losses,” *IEEE Trans. Power Electron.*, vol. 34, no. 2, pp. 1518–1525, Feb. 2019.

[35] M. M. Swamy, J. K. Kang, and K. Shirabe, “Power loss, system efficiency, and leakage current comparison between Si IGBT VFD and SiC FET VFD with various filtering options,” *IEEE Trans. Ind. Appl.*, vol. 51, no. 5, pp. 3858–3866, Sep./Oct. 2015.

[36] T. Hoshino, Y. Okuyama, E. Tanaka, and T. Kai, “Analytical solution for steady State characteristics of permanent magnet field synchronous motor,” in *Proc. 23rd Int. Conf. Elect. Mach. Syst.*, 2020, pp. 1564–1567.

[37] X. C. Wang et al., “Torque ripple reduction in sectored multi three-phase machines based on PWM carrier phase shift,” *IEEE Trans. Ind. Electron.*, vol. 67, no. 6, pp. 4315–4325, Jun. 2020.

[38] S. G. Jeong and M. H. Park, “The analysis and compensation of dead-time effects in PWM inverters,” *IEEE Trans. Ind. Electron.*, vol. 38, no. 2, pp. 108–114, Apr. 1991.

[39] G. Sala, M. Mengoni, G. Rizzoli, L. Zarri, and A. Tani, “Decoupled d-q axes current-sharing control of multi-three-phase induction machines,” *IEEE Trans. Ind. Electron.*, vol. 67, no. 9, pp. 7124–7134, Sep. 2020.

[40] I. Zoric, M. Jones, and E. Levi, “Arbitrary power sharing among three-phase winding sets of multiphase machines,” *IEEE Trans. Ind. Electron.*, vol. 65, no. 2, pp. 1128–1139, Feb. 2018.

[41] B. H. Bae and S. K. Sul, “A compensation method for time delay of full-digital synchronous frame current regulator of PWM AC drives,” *IEEE Trans. Ind. Appl.*, vol. 39, no. 3, pp. 802–810, May/Jun. 2003.

[42] B. Y. Zheng, J. B. Zou, Y. X. Xu, X. Y. Lang, and G. D. Yu, “Torque ripple suppression based on optimal harmonic current injection in dual three-phase PMSMs under magnetic saturation,” *IEEE Trans. Ind. Electron.*, vol. 69, no. 6, pp. 5398–5408, Jun. 2022.

[43] J. Holtz, “Pulsewidth modulation - a survey,” *IEEE Trans. Ind. Electron.*, vol. 39, no. 5, pp. 410–420, Oct. 1992.

[44] L. J. Wu and Z. K. Lyu, “Harmonic injection-based torque ripple reduction of PMSM with improved DC-link voltage utilization,” *IEEE Trans. Power Electron.*, vol. 38, no. 7, pp. 7976–7981, Jul. 2023.

Shusen Ni (Student Member, IEEE) was born in Shandong, China, in 2000. He received the B.S. degree in electrical engineering from Shandong University, Jinan, China, in 2022. He is currently working toward the Ph.D. degree in power electronics and electrical drives with the State Key Laboratory of Power System, Department of Electrical Engineering, Tsinghua University Beijing, China.

His current research interests include high performance control and fault tolerant control of multiphase machine drives.

Chi Li (Member, IEEE) received the B.S. degree from Tsinghua University, Beijing, China, in 2012, and the M.S. and Ph.D. degrees from Virginia Tech, Blacksburg, VA, USA, in 2015 and 2018, respectively, all in electrical engineering.

From 2012 to 2018, he was a Research Assistant with the Center for Power Electronics Systems, Virginia Tech. In 2018, he returned to Tsinghua University and he is currently an Assistant Researcher with the Department of Electrical Engineering, Tsinghua University. His research interests include control and stability of power electronics converters and systems.

Zedong Zheng (Senior Member, IEEE) was born in Shandong, China, in 1980. He received the B.S. and Ph.D. degrees in electrical engineering from the Department of Electrical Engineering, Tsinghua University, Beijing, China, in 2003 and 2008, respectively.

He is currently an Associate Professor with Department of Electrical Engineering, Tsinghua University. His current research interests include power electronics converters and high-performance motor control systems.